SELF-ADAPTIVE ABSORBING BOUNDARY CONDITIONS FOR QUASILINEAR ACOUSTIC WAVE PROPAGATION

Markus Muhr*, Vanja Nikolić, and Barbara Wohlmuth

Technical University of Munich, Department of Mathematics, Chair of Numerical Mathematics
Boltzmannstraße 3, 85748 Garching, Germany

Abstract. We propose a self-adaptive absorbing technique for quasilinear ultrasound waves in two- and three-dimensional computational domains. As a model for the nonlinear ultrasound propagation in thermoviscous fluids, we employ Westervelt's wave equation solved for the acoustic velocity potential. The angle of incidence of the wave is computed based on the information provided by the wave-field gradient which is readily available in the finite element framework. The absorbing boundary conditions are then updated with the angle values in real time. Numerical experiments illustrate the accuracy and efficiency of the proposed method.

1. Introduction

Accurate simulation of nonlinear ultrasound offers a path to a better quality of many procedures in industry and medicine, from non-destructive detection of material damages [8, 25, 42] to non-invasive treatments of medical disorders [24, 35, 36, 62, 66]. When studying such procedures, there is always a region of interest: a kidney stone that will be disintegrated or a propagating fatigue crack in a component of an aircraft. The large physical space then often has to be truncated for numerical simulations. To accurately simulate ultrasound, we have to avoid spurious reflections of the wave at the boundary of the truncated domain.

Absorbing boundary conditions provide a simple and effective way of dealing with unwanted reflections. They were introduced by B. Engquist and E. Majda in their seminal work [7]. Since then many approaches have been developed for the non-reflecting boundary conditions; we refer the reader to the review papers [12, 46] and the references given therein. In spite of such comprehensive research in this area, only a small portion of the results focus on nonlinear models.

A class of semilinear wave equations and nonlinear Schrödinger equations was investigated in [56, 57]. Results for nonlinear hyperbolic systems of the form $u_t + A(u)u_x = 0$ were obtained in [16]. An approach based on the operator splitting method was used in [39] to derive absorbing conditions for a semilinear wave equation of the form $u_{tt} - a^2 \Delta u = f(u)$. In [52, 53], nonlinear ultrasound propagation was investigated in this context for the first time, and absorbing conditions were developed for the Westervelt equation in the pressure form.

Another commonly used approach for avoiding spurious reflections is the Perfectly Matched Layer (PML) technique. Developed by J.-P. Bérenger in [2], this method introduces an artificial absorbing layer around the computational domain. Linear acoustic wave equations have been extensively studied in this context; see, for example, [1, 17, 18, 29, 49].

The main downside of absorbing conditions is that they are sensitive to the angle of incidence of the wave. As a rule of thumb, they perform bad if the range of incidence angles is large. The information on the incidence angles can be included in the conditions to tackle this issue; we refer to the work in [19, 20, 37]. However, these angles are not a priori known in a realistic computational setting.

The idea behind the self-adaptive technique is to compute the local wave vector and then update the absorbing conditions with the angle information *in real time*. This approach was applied in [63] to the Schrödinger-type equations, where the wave number was computed via the Gabor transform. In [54], the linear wave equation was investigated in this context. It was proposed to divide the absorbing boundary into segments and compute the local incidence angle by employing the Fourier transformation only in the vicinity of the boundary. The self-adaptive approach to absorption can also be found in earlier works on acoustic scattering [27, 40].

The goal of our work is to develop an efficient self-adaptive absorbing technique for nonlinear ultrasound propagation. As a model equation, we employ a classical quasilinear acoustic model - Westervelt's equation. We first extend the results from [52, 53] by considering the potential form of Westervelt's equation and the non-zero angle of incidence θ. In addition, we derive the absorbing conditions for two- and three-dimensional computational domains. The derivation relies on choosing an appropriate linearization of the equation around a reference solution. The absorbing conditions are then formally derived for this linearization, after which we bring back the nonlinear term.

To obtain the angle θ in practice, we develop a self-adaptive method that locally computes the incidence angle and updates the absorbing conditions on the fly. Unlike the self-adaptive approach taken in [54], we base the local angle computation on the gradient of the wave field. Computation of the local propagation direction in isotropic media based on the information provided by the wave-field gradient has been investigated in [26, 48, 51, 64, 65, 67]. This approach is particularly suitable for our finite-element framework since the gradient information is already available at every time step in our simulations. The use of the field gradient information in the absorbing conditions was already investigated for the Helmholtz equation in [13]. There it was proposed to replace the normal derivatives that appear in the absorbing conditions by the derivatives in the direction of the wave propagation. In the linear regime, our approach can be understood as an extension of the gradient method in [13] for a time-dependent wave model.

We organize the rest of the paper as follows. We begin in Section 2 by introducing the model and setting the problem. Section 3 contains the derivation of absorbing conditions for a given angle of incidence of the wave. In Section 4, we present the numerical scheme for solving the initial-boundary value problem for the Westervelt equation. Section 5 describes the computation of the local incidence angle via the information provided by the wave field gradient. Finally, in Section 6, we present numerical experiments which illustrate the accuracy of the proposed adaptive boundary conditions.

2. Modeling and problem setting

The weakly nonlinear models in thermoviscous acoustics that are commonly used are obtained as an approximation of the compressible Navier-Stokes system. We here briefly reflect upon the derivation, which will give us a better understanding of the often-employed Westervelt equation. Mathematically rigorous justification of the classical acoustic models can be found in [32]. For a detailed insight into the acoustic field theory, we refer to [5, 15, 33].

Propagation of waves can be described by the time, the density $\bar{\varrho}$, the pressure $\bar{u}$ and the velocity $\bar{\mathbf{v}}$, decomposed into their ambient value and the acoustic perturbation

$$\bar{\varrho} = \varrho_0 + \varrho,$$
$$\bar{u} = u_0 + u,$$
$$\bar{\mathbf{v}} = \mathbf{v}_0 + \mathbf{v};$$

see [33]. We call ϱ the acoustic density, u the acoustic pressure, and $\mathbf{v}$ the acoustic particle velocity. The equations governing the wave propagation are then given by

- the equation of momentum conservation

$$(\varrho_0 + \varrho)\mathbf{v}_t + \frac{\varrho_0}{2}\nabla(\mathbf{v} \cdot \mathbf{v}) + \nabla u = \left(\frac{4\nu_V}{3} + \eta_V\right)\Delta\mathbf{v},$$

- the equation of mass conservation

$$\varrho_t + \varrho_0\nabla \cdot \mathbf{v} = -\varrho\nabla \cdot \mathbf{v} - \mathbf{v} \cdot \nabla\varrho,$$

- the pressure-density relation

$$\varrho = \frac{1}{c^2}u - \frac{1}{\varrho_0 c^4}\frac{B}{2A}u^2 - \frac{\kappa}{\varrho_0 c^4}\left(\frac{1}{c_\Omega} - \frac{1}{c_u}\right)u_t.$$

Above, η_V denotes the bulk viscosity and ν_V the shear viscosity. The constant κ stands for the adiabatic exponent, c_u and c_Ω denote the specific heat capacitance at constant pressure and constant volume, respectively. The parameter of nonlinearity B/A is an indicator of the nonlinearity of the medium. Finally, c denotes the speed of sound in the fluid.

This system of equations is approximated by one model, whereby every term of order two and higher in the acoustic Mach number is neglected. This approach results in

$$(1) \quad \begin{cases} \frac{1}{c^2}u_{tt} - \Delta u - \frac{b}{c^2}\Delta u_t = \frac{1}{\varrho_0 c^4}\frac{B}{2A}u_{tt} + \frac{\varrho_0}{c^2}\frac{\partial^2}{\partial t^2}(\mathbf{v}\cdot\mathbf{v}), \\ \varrho_0\mathbf{v}_t = -\nabla u, \end{cases}$$

where the so-called sound diffusivity b is given by

$$b = \frac{1}{\varrho_0}\left(\frac{4\nu_V}{3} + \eta_V\right) + \frac{\kappa}{\varrho_0}\left(\frac{1}{c_V} - \frac{1}{c_u}\right).$$

The acoustic velocity potential ψ is then introduced to obtain a scalar equation; it is related to the acoustic pressure by

$$(2) \quad u \approx \varrho_0\psi_t,$$

and to the acoustic particle velocity by

$$(3) \quad \mathbf{v} = -\nabla\psi.$$

By expressing (1) in terms of ψ, integrating with respect to time and taking the resulting constant of integration to be zero, we arrive at the Kuznetsov equation

$$(4) \quad \frac{1}{c^2}\psi_{tt} - \Delta\psi - \frac{b}{c^2}\Delta\psi_t = \frac{B/A}{c^4}\psi_t\psi_{tt} + \frac{2}{c^2}\nabla\psi\cdot\nabla\psi_t;$$

cf. [38]. If the cumulative nonlinear effects dominate the local ones in the sense of

$$(5) \quad \frac{2}{c^2}\nabla\psi\cdot\nabla\psi_t \approx \frac{2}{c^2}\psi_t\psi_{tt},$$

a simplification of (4), known as the Westervelt equation [60], is obtained

$$(6) \quad \frac{1}{c^2}\psi_{tt} - \Delta\psi - \delta\Delta\psi_t = \frac{k}{c^2}\psi_t\psi_{tt}.$$

Above we have introduced the notation

$$(7) \quad \delta = \frac{b}{c^2}, \; k = \frac{1}{c^2}(B/A + 2).$$

After numerically solving (6), the pressure field can be obtained in a post-processing step via the relation (2). We mention as well that the Westervelt equation in the pressure form is given by

$$(8) \quad \frac{1}{c^2}u_{tt} - \Delta u - \delta\Delta u_t = \frac{k}{\varrho c^2}\left(uu_{tt} + u_t^2\right).$$

Equation (8) can be obtained from (1) by employing the approximation (5) which in terms of the velocity and pressure reads as

$$\frac{\varrho_0}{2}\mathbf{v}\cdot\mathbf{v} \approx \frac{u^2}{2\varrho_0 c^2}.$$

3. Absorbing conditions for the Westervelt equation

We consider the Westervelt equation (6) on a three-dimensional spatial domain $\Omega = \{(x, y, z) : x < 0, y, z \in \mathbb{R}\}$. We restrict ourselves in the problem description to the case of constant coefficients c, b, and k

3.1. Linearization of the Westervelt equation.

Following the approach from [52] where equation (8) was considered, we derive absorbing conditions for the Westervelt equation in the potential form (6) by first transforming it into a linear equation, deriving the non-reflecting conditions for this linear model and then "plugging" back in the nonlinear term.

It is clear that the linearization of the equation plays a crucial role in deriving the absorbing conditions. A possible linearization of the Westervelt equation around a reference solution ψ^{ref} is given by

$$(9) \qquad \frac{1}{c^2}\psi_{tt} - \Delta\psi - \delta\Delta\psi_t = \frac{k}{c^2}\beta(x, y, z, t)\,\psi_{tt},$$

where $\beta = \psi_t^{\mathrm{ref}}$. We note that, unlike in the derivation of the Westervelt equation in Section 2, here we do not split ψ into a background and oscillatory part, instead we assume ψ^{ref} to be a solution of the equation. This linearization is analogous to the one employed in [52] for the equation in the pressure formulation (8).

We propose an alternative linearization. Note that the right-hand side of the Westervelt equation (6) can be rewritten as $\frac{1}{2}\frac{k}{c^2}(\psi_t^2)_t$. We linearize the term ψ_t^2 as $\psi_t^{\mathrm{ref}}\psi_t$ and study the following equation

$$(10) \qquad \frac{1}{c^2}\psi_{tt} - \Delta\psi - \delta\Delta\psi_t = \frac{1}{2}\frac{k}{c^2}(\beta(x, y, z, t)\psi_t)_t,$$

where again $\beta = \psi_t^{\mathrm{ref}}$. The absorbing boundary conditions based on linearizations (9) and (10) are numerically compared in Section 6.

We first derive absorbing conditions for the linear equation (10) and a given angle of incidence. After obtaining the conditions for such a model, the coefficient β is set back to ψ_t to obtain nonlinear conditions.

We remark that the linearization via Taylor expansion around a reference solution ψ^{ref} is not considered here since it would introduce the term $\psi_t^{\mathrm{ref}}\psi_{tt}^{\mathrm{ref}}$ into the linearized equation; we also refer to the discussion in [52].

3.2. Derivation of absorbing conditions for the angle of incidence θ.

We study here the derivation of the absorbing conditions for the linearization (10); equation (9) can be treated analogously. To derive the conditions, we could use the frozen coefficient approach which first transforms the variable coefficient equation into its constant-coefficient counterpart by "freezing" its coefficients at a given point before employing the Fourier transform in the (y, z, t) coordinates; cf. [7, Section 1]. Although the main focus of the present work is the derivation of the zero-order (adaptive) absorbing conditions, we still follow the approach based on the pseudo-differential calculus since it allows to arrive at a general system for determining the correcting terms beyond order zero in the absorbing conditions; see system (19) below.

We first rewrite the linearized equation (10) in the operator form as

$$(11) \qquad \mathcal{P}u = 0,$$

where the operator $\mathcal{P}$ is given by

$$(12) \quad \mathcal{P} = \left(\frac{1}{c^2} - \frac{1}{2}\frac{k}{c^2}\beta(x, y, z, t)\right)\partial_t^2 - \partial_x^2 - \partial_y^2 - \partial_z^2 - \delta\partial_x^2\partial_t - \delta\partial_y^2\partial_t - \delta\partial_z^2\partial_t - \frac{1}{2}\frac{k}{c^2}\beta_t(x, y, z, t)\partial_t.$$

At this point we also introduce

$$
\begin{aligned}
\alpha_0(x,y,z,t) &= \sqrt{\frac{1}{c^2} - \frac{1}{2}\frac{k}{c^2}\beta(x,y,z,t)}, \\
\alpha_1(x,y,z,t) &= \frac{1}{2}\frac{k}{c^2}\beta_t(x,y,z,t).
\end{aligned}
\tag{13}
$$

Note that the well-posedness results for the Westervelt equation rely on the fact that the factor $1 - k\psi_t$ next to the second time derivative remains positive; see [30, 31, 34]. Therefore, it is reasonable to assume that the term under the square root in (13) is positive for sufficiently small data. We note that we proceed heuristically since the rigorous justification of the derivations given below would also require C^∞ regularity of α_0 and α_1 which is not proven here.

Absorbing boundary conditions for (11) can be derived by employing the pseudo-differential calculus and factorization of the operator $\mathcal{P}$ according to L. Nirenberg's procedure [47, Chapter II]. We briefly summarize the procedure here for the convenience of the reader. A detailed account on the pseudo-differential operators can be found in [22, 47, 61].

Definition 1. [23, 61] *Let the set $\mathcal{S}^m$, where $m \in \mathbb{R}$, be defined as the set of all functions $q(t,\tau) \in C^\infty(\mathbb{R}^d \times \mathbb{R}^d)$ such that for any two multi-indices k and l, there is a positive constant C_{kl} depending only on k and l, such that*

$$
|\partial_t^k \partial_\tau^l q(t,\tau)| \le C_{kl}(1+|\tau|)^{m-|l|}, \quad t, \tau \in \mathbb{R}^d.
$$

$\mathcal{S}^m$ is called the space of symbols of order m. We set $S^{-\infty} = \cap_{m \in \mathbb{R}}\mathcal{S}^m$.

Definition 2. [61, Definition 5.2] *Let q be a symbol. The pseudo-differential operator $\mathcal{Q}$ associated to q is defined by*

$$
(\mathcal{Q}\varphi)(t) = (2\pi)^{-d/2}\int_{\mathbb{R}^d} e^{it\cdot\tau}\,q(t,\tau)\,\mathcal{F}\varphi(\tau)\,d\tau,
$$

where φ is a function from the Schwartz space, and $\mathcal{F}$ denotes the Fourier transform.

3.2.1. *Propagation without losses.* Following the approach in [52], we first derive the absorbing conditions with the assumption that $\delta = 0$. This assumption facilitates the derivation of the conditions based on the pseudo-differential factorization. The δ-term will be included as a post-processing step based on energy arguments.

The derivation of the conditions relies on the fact that the operator $\mathcal{P}$ can be factorized into in the form

$$
\mathcal{P} = -\left(\partial_x - \mathcal{A}\left(x,y,z,t,\partial_y,\partial_z,\partial_t\right)\right)\left(\partial_x - \mathcal{B}\left(x,y,z,t,\partial_y,\partial_z,\partial_t\right)\right) + \mathcal{R}\left(x,y,z,t,\partial_y,\partial_z,\partial_t\right);
\tag{14}
$$

see [47, Lemma 1]. In (14), the operators $\mathcal{A}$ and $\mathcal{B}$ are pseudo-differential operators with the symbols $a(x,y,z,t,\eta,\zeta,\tau)$ and $b(x,y,z,t,\eta,\zeta,\tau)$, respectively, from the space $\mathcal{S}^1$. The conditions on $\mathcal{A}$ that we will develop will have the effect of associating $\mathcal{A}$ with waves that travel out of the computational domain. The pseudo-differential operator $\mathcal{R}$ is a smoothing operator with the full symbol $r(x,y,z,t,\eta,\zeta,\tau)$ that belongs to $\mathcal{S}^{-\infty}$.

The symbols a and b formally admit asymptotic expansions

$$
\begin{aligned}
a(x,y,z,t,\eta,\zeta,\tau) &\sim \sum_{j\ge 0} a_{1-j}(x,y,z,t,\eta,\zeta,\tau), \\
b(x,y,z,t,\eta,\zeta,\tau) &\sim \sum_{j\ge 0} b_{1-j}(x,y,z,t,\eta,\zeta,\tau),
\end{aligned}
$$

where a_{1-j} and b_{1-j} denote homogeneous functions of degree $1-j$ with respect to τ; see [61, Theorem 5.10]. We note that the symbol $a(x,y,z,t,\eta,\zeta,\tau)b(x,y,z,t,\eta,\zeta,\tau)$ of the product of A and B has an asymptotic expansion as well

$$
a(x,y,z,t,\eta,\zeta,\tau)b(x,y,z,t,\eta,\zeta,\tau) \sim \sum_{\substack{j\ge 0, \\ k+l+n=j, \\ k,l,n\ge 0}} \frac{(-1)^n}{n!}\partial_\tau^n a_{1-l}(x,y,z,t,\eta,\zeta,\tau)\partial_t^n b_{1-k}(x,y,z,t,\eta,\zeta,\tau);
$$

see [61, Theorem 7.1].

According to [41, Theorems 1 and 2], absorbing boundary conditions on the boundary $x = 0$ are given in the form

$$\left(\partial_x - \mathcal{A}\left(x, y, z, t, \partial_y, \partial_z, \partial_t\right)\right) \psi\Big|_{x=0} = 0.$$

Since the symbol a of A has an infinite expansion, in numerical simulations this expansion is truncated after a certain number of terms. Absorbing conditions of order $k \in \mathbb{N}_0$ are then on the symbolic level given by

$$(15) \qquad \left(\partial_x - \sum_{j=0}^{k} a_{1-j}(0, y, z, t, \eta, \zeta, \tau)\right) \psi\Big|_{x=0} = 0.$$

The higher-order absorbing conditions, although numerically more accurate, are also significantly more involved when it comes to implementation. We compute the absorbing conditions of order zero for the given angle of incidence θ. Combined with the proposed self-adaptive technique, this approach allows to improve the accuracy of zero-order conditions, yet keeps them easy to implement.

We recall how the operator $\mathcal{P}$ was defined in (12) and then develop factorization (14) to obtain

$$(16) \qquad \begin{aligned} &\alpha_0^2\, \partial_t^2 - \partial_x^2 - \partial_y^2 - \partial_z^2 - \alpha_1 \partial_t \\ &= -\partial_x^2 + (\mathcal{A} + \mathcal{B})\partial_x + \mathcal{B}_x - \mathcal{A}\mathcal{B} + \mathcal{R}. \end{aligned}$$

By employing the asymptotic expansion of symbols a, b, and ab, equation (16) reduces on the symbolic level to

$$(17) \qquad \begin{aligned} &\alpha_0^2(i\tau)^2 - (i\eta)^2 - (i\zeta)^2 - \alpha_1(i\tau) \\ &\cong \sum_{j \geq 0}(a_{1-j} + b_{1-j})\partial_x + \sum_{j \geq 0} \partial_x b_{1-j} - \sum_{\substack{j \geq 0, \\ k+l+n=j, \\ k,l,n \geq 0}} \frac{(-1)^n}{n!}\partial_\tau^n a_{1-l}\partial_t^n b_{1-k}, \end{aligned}$$

Above, we have denoted the dual variables to t, y, and z by τ, η, and ζ, with the correspondence $\partial_t \leftrightarrow i\tau$, $\partial_y \leftrightarrow i\eta$, and $\partial_z \leftrightarrow i\zeta$. Following the notation in [7], $\cong$ stands for "within a smooth error" since we have dropped $\mathcal{R}$. We note that the operator R can only be controlled in terms of its smoothness. However, its action on the solution is expected to be negligible for high frequencies that are present in ultrasound waves.

To determine a_1 and b_1, we equate the symbols with the same degree of homogeneity with respect to τ and get the system

$$(18) \qquad \begin{cases} a_1 + b_1 = 0 \\ a_1 b_1 = -(\alpha_0^2(i\tau)^2 - (i\eta)^2 - (i\zeta)^2), \end{cases}$$

assuming that $\alpha_0^2 \tau^2 \cong \eta^2 + \zeta^2$. The system that determines the coefficients $\{a_{1-j}, b_{1-j}\}_{j \geq 1}$ is then given by

$$(19) \qquad \begin{cases} a_{1-j} + b_{1-j} = 0, \qquad j \geq 1, \\ -\alpha_1(i\tau)\delta_{j1} = -\sum_{\substack{j \geq 1, \\ k+l+n=j, \\ k,l,n \geq 0}} \frac{(-1)^n}{n!}\partial_\tau^n a_{1-l}\partial_t^n b_{1-k} + \partial_x b_{1-j}, \end{cases}$$

where δ denotes the Kronecker delta. From (18), we find that

$$a_1 = -\sqrt{\alpha_0^2(i\tau)^2 - (i\eta)^2 - (i\zeta)^2}$$

and

$$b_1 = \sqrt{\alpha_0^2(i\tau)^2 - (i\eta)^2 - (i\zeta)^2}.$$

Note that the sign of a_1 determines the propagation direction of the wave. To obtain the absorbing conditions for the given angle of incidence, we freeze the coefficient β in (12) by assuming that it is constant in space and time. The dispersion relation for (10) when β is constant is as follows

$$(20) \qquad \alpha_0^2(i\tau)^2 - (i\xi)^2 - (i\eta)^2 - (i\zeta)^2 = 0.$$

The wave vector is given by (ξ, η, ζ). If we denote by $\theta \in [0\,^\circ, 90\,^\circ]$ the angle between the incident wave and the outer normal to the boundary, we have for $\tau > 0$

$$\sin\theta = \frac{\sqrt{\eta^2 + \zeta^2}}{\sqrt{\xi^2 + \eta^2 + \zeta^2}} = \frac{\sqrt{\eta^2 + \zeta^2}}{\alpha_0 \tau};$$

see Figure 1.
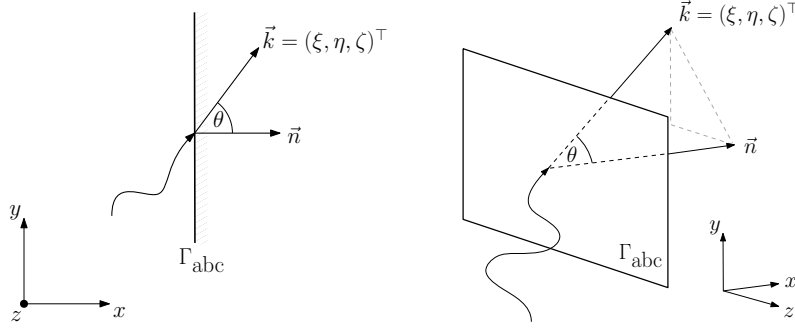
FIGURE 1. Illustration of the interplay between the wave vector $\vec{k}$, outward normal vector $\vec{n}$, and the angle of incidence θ.

Therefore, we can express a_1 as

$$a_1 = -\alpha_0(i\tau)\sqrt{1 - \frac{\eta^2 + \zeta^2}{\alpha_0^2 \tau^2}} = -\alpha_0(i\tau)\cos\theta.$$

According to (15), the absorbing conditions of order zero are then given by

$$(21) \qquad \frac{\partial\psi}{\partial n} = -\alpha_0\,\psi_t \cos\theta.$$

We mention that for a variable coefficient problem with jumps outside the computational domain, it is not possible to build an exact ABC based on local computations. After returning to $\beta = \psi_t$ and $\alpha_0 = \sqrt{\dfrac{1}{c^2} - \dfrac{1}{2}\dfrac{k}{c^2}\psi_t}$, we obtain the absorbing boundary conditions for the inviscid Westervelt equation in the potential formulation for a given angle of incidence θ:

$$(22) \qquad c\frac{\partial\psi}{\partial n} + \sqrt{1 - \frac{k}{2}\psi_t}\,\psi_t \, \cos\theta = 0.$$

3.2.2. *Propagation with losses.* We next want to incorporate the b term into the conditions. This was not possible before since we needed $b = 0$ to make use of the pseudo-differential factorization and the dispersion relation (20). Instead, we employ a reasoning based on an energy argument.

To this end, we test the linearized equation (10) with ψ_t, integrate over space and $(0, t)$, where $t \leq T$, and integrate by parts with respect to time, to arrive at the following identity:

$$(23) \qquad \begin{aligned} &E_0[\psi](t) + \delta\int_0^t \|\nabla\psi_t\|_{L^2(\Omega)}^2 \,\mathrm{d}s \\ &= E_0[\psi](0) + \int_0^t\int_\Omega \left(\tfrac{1}{2}(\alpha_0^2)_t + \alpha_1\right)\psi_t^2 \,\mathrm{d}x\mathrm{d}s + \int_0^t\int_{\partial\Omega}\left(\frac{\partial\psi}{\partial n} + \delta\frac{\partial\psi_t}{\partial n}\right)\psi_t \,\mathrm{d}x\mathrm{d}s, \end{aligned}$$

where the energy is given by

$$E_0[\psi](t) = \frac{1}{2}\left(\|\alpha_0(t)\psi_t(t)\|^2_{L^2(\Omega)} + \|\nabla\psi(t)\|^2_{L^2(\Omega)}\right).$$

This identity suggests to modify the conditions (21) to include the sound diffusivity as follows

$$(24) \qquad \frac{\partial\psi}{\partial n} + \delta\frac{\partial\psi_t}{\partial n} = -\alpha_0\,\psi_t\cos\theta \quad \text{on } \Gamma_{\text{abc}}.$$

These conditions facilitate the extraction of energy through the boundary since (23) becomes

$$(25) \qquad \begin{aligned} &E_0[\psi](t) + \delta\int_0^t \|\nabla\psi_t\|^2_{L^2(\Omega)}\,\mathrm{d}s + \int_0^t \left\|\sqrt{\alpha_0\cos\theta}\,\psi_t\right\|^2_{L^2(\partial\Omega)}\,\mathrm{d}s \\ &= E_0[\psi](0) + \int_0^t\int_\Omega (\tfrac{1}{2}(\alpha_0^2)_t + \alpha_1)\psi_t^2\,\mathrm{d}x\mathrm{d}s, \end{aligned}$$

from which by employing Gronwall's inequality it follows that

$$E_0[\psi](t) + \delta\int_0^t \|\nabla\psi_t\|^2_{L^2(\Omega)}\,\mathrm{d}s + \int_0^t \left\|\sqrt{\alpha_0\cos\theta}\,\psi_t\right\|^2_{L^2(\partial\Omega)}\,\mathrm{d}s \le C(T)E_0[\psi](0),$$

provided $\frac{1}{2}(\alpha_0^2)_t + \alpha_1 \in L^\infty(0,T; L^\infty(\Omega))$.

We therefore adopt conditions (24). After returning to $\beta = \psi_t$ and $\alpha_0 = \sqrt{\frac{1}{c^2} - \frac{1}{2}\frac{k}{c^2}\psi_t}$ in (24) and recalling that $\delta = b/c^2$, we obtain the nonlinear conditions

$$(26) \qquad c^2\frac{\partial\psi}{\partial n} + b\frac{\partial\psi_t}{\partial n} = -c\sqrt{1 - \frac{k}{2}\psi_t}\,\psi_t\cos\theta \quad \text{on } \Gamma_{\text{abc}}.$$

We note that in realistic settings the sound diffusivity b in fluids is small; see, e.g., [33]. It is also known that the presence of a large b damping in the model would imply a parabolic instead of a wave-like behavior of the equation resulting in an exponential decay of the energy; cf. [30, Theorem 3.3].

Setting k to zero in (26) corresponds to conditions for a linear, strongly damped wave equation. If in addition $b = 0$, we end up with the standard linear absorbing conditions for the angle θ

$$(27) \qquad c\frac{\partial\psi}{\partial n} + \psi_t\cos\theta = 0 \quad \text{on } \Gamma_{\text{abc}};$$

see [19, 37].

Remark 1 (One- and two-dimensional domains). *In a one-dimensional setting, system* (18) *for determining the symbols a_1 and b_1 simplifies to*

$$\begin{cases} a_1 + b_1 = 0 \\ a_1 b_1 = -\alpha_0^2(i\tau)^2. \end{cases}$$

In a two-dimensional setting, system (18) *simplifies to*

$$\begin{cases} a_1 + b_1 = 0 \\ a_1 b_1 = -(\alpha_0^2(i\tau)^2 - (i\eta)^2). \end{cases}$$

It is then straightforward to show that conditions (26) *hold in 1D and 2D as well, where in 1D the angle θ can be interpreted as being set to $\theta = 0°$.*

Remark 2 (A different linearization). *Employing linearization* (9) *would result in the following absorbing conditions*

$$(28) \qquad c^2\frac{\partial\psi}{\partial n} + b\frac{\partial\psi_t}{\partial n} = -c\sqrt{1 - k\psi_t}\,\psi_t\cos\theta \quad \text{on } \Gamma_{\text{abc}}.$$

The performance of conditions (26) *and* (28) *is compared in Section* 6, *where the proposed conditions* (26) *significantly outperform* (28).

Remark 3. *In our experiments, we employ the gradient information to compute the angle of incidence* θ *via*

$$\cos\theta = \frac{|\nabla\psi \cdot n|}{\sqrt{\psi_x^2 + \psi_y^2 + \psi_z^2}} \quad \text{on } \Gamma_{\text{abc}},$$

assuming that $\nabla\psi \neq 0$ *on the absorbing boundary. The linear conditions* (27) *for the angle* θ *are then equivalent to*

$$(29) \qquad c|\nabla\psi| + \psi_t = 0 \quad \text{on } \Gamma_{\text{abc}}.$$

Therefore, in the linear regime, conditions (29) *can be seen as the extension of the absorbing conditions proposed in* [13] *for the Helmholtz equation to the linear time-dependent wave model.*

4. NUMERICAL TREATMENT

After deriving the absorbing boundary conditions for the potential form of the Westervelt equation (6), we next focus on the numerical schemes used in simulations. We begin by formulating the initial-boundary value problem that has to be solved.

4.1. **The initial-boundary value problem for the Westervelt equation.** We consider the following problem for the Westervelt equation:

$$(30) \qquad \begin{cases} \psi_{tt} - c^2\Delta\psi - b\Delta\psi_t = \dfrac{1}{c^2}(B/A + 2)\,\psi_t\psi_{tt} & \text{in } \Omega \times (0,T), \\[2mm] \psi = g & \text{on } \Gamma_{\text{exc}} \times (0,T), \\[2mm] c\dfrac{\partial\psi}{\partial n} + \dfrac{b}{c}\dfrac{\partial\psi_t}{\partial n} = -\sqrt{1 - \sigma k\psi_t}\,\psi_t\cos\theta(\psi) & \text{on } \Gamma_{\text{abc}} \times (0,T), \\[2mm] \dfrac{\partial\psi}{\partial n} = 0 & \text{on } \Gamma_{\text{N}} \times (0,T), \\[2mm] \psi = \psi_t = 0 & \text{in } \Omega \times \{0\}. \end{cases}$$

The wave source is given in the form of inhomogeneous Dirichlet conditions on the excitation part of the domain boundary $\Gamma_{\text{exc}} \subset \partial\Omega$. In our numerical tests, the excitation signal is always taken to be a modulated sine wave, that is growing over time until its maximal amplitude is reached, i.e.

$$(31) \qquad g(t) = \begin{cases} (f^2/4)t^2\mathfrak{A}\sin(\omega t), & t < 2/f, \\[2mm] \mathfrak{A}\sin(\omega t), & t \geq 2/f, \end{cases}$$

where f denotes the frequency, $\omega = 2\pi f$ the angular frequency, and $\mathfrak{A}$ the maximal amplitude of the signal.

We have introduced the parameter σ within the square root of the absorbing conditions in (30). In this way, we generalized in one formula all the absorbing conditions that we want to compare. Indeed, setting $\sigma = 0$ yields the adaptive absorbing conditions for the linear strongly damped wave equation

$$(32) \qquad c\frac{\partial\psi}{\partial n} + \frac{b}{c}\frac{\partial\psi_t}{\partial n} = -\psi_t\cos\theta(\psi),$$

which we denote from now on in experiments by "ABC$_{\text{W}}^0$ adaptive". In case also $\theta = 0$ everywhere, we denote them just by ABC$_{\text{W}}^0$. Setting $\sigma = 1/2$ recovers our new nonlinear adaptive conditions, denoted by "ABC$_{\text{W}}^{1/2}$ adaptive". If the angle is always set to zero, we denote them just by ABC$_{\text{W}}^{1/2}$. Finally, $\sigma = 1$ leads to conditions based on the second linearization (9), which are denoted in the experiments by "ABC$_{\text{W}}^1$ adaptive" and ABC$_{\text{W}}^1$.

We start from the weak form of the problem (30). We are looking for a solution in

$$\{\psi \in C^1([0,T]; H^2(\Omega)) \cap C^2([0,T]; H^1(\Omega)) \,|\, \psi = g \text{ on } \Gamma_{\text{exc}} \times (0,T)\}$$

such that

$$\int_\Omega ((1 - k\psi_t)\psi_{tt}v + c^2\nabla\psi \cdot \nabla v + b\nabla\psi_t \cdot \nabla v)\, \mathrm{d}\Omega + \int_{\Gamma_{\mathrm{abc}}} c\,\sqrt{1 - \sigma k\psi_t}\,\psi_t\,\cos\theta(\psi)\,v\,\mathrm{d}S = 0$$

for all test functions in $\{v \in H^1(\Omega)\,|\,v = 0 \text{ on } \Gamma_{\mathrm{exc}} \times (0,T)\}$ a.e. in time, with $(\psi, \psi_t)|_{t=0} = (0,0)$. We assume that the problem (30) is well-posed, although the rigorous proof is beyond the scope of the current work. Results on the well-posedness of the Westervelt equation in the pressure form with nonlinear absorbing conditions for the angle of incidence $\theta = 0°$ can be found in [53, 55].

4.2. **Finite element discretization and time integration.** We follow the standard discretization methods for nonlinear acoustics based on finite elements [10, 21, 28, 33, 43, 58]. The finite element method is employed in space with lowest order conforming elements on simplicial meshes.

The mass $\mathbf{M}$, stiffness $\mathbf{K}$, and damping matrix $\mathbf{C}$ as well as the nonlinearity tensor $\boldsymbol{\mathcal{T}}$ are assembled in the usual manner; see [33, 43]. By dividing the set of degrees of freedom into the set of Dirichlet degrees D and the set of interior degrees I, the semi-discrete problem reads as follows

(33)
$$\begin{cases} \mathbf{M}_{\mathrm{I,I}}\underline{\ddot{\psi}}_{\mathrm{I}} + \mathbf{K}_{\mathrm{I,I}}\underline{\psi}_{\mathrm{I}} + \mathbf{C}_{\mathrm{I,I}}\underline{\dot{\psi}}_{\mathrm{I}} - \boldsymbol{\mathcal{T}}_{\mathrm{I,I,I}}[\underline{\ddot{\psi}}_{\mathrm{I}}, \underline{\dot{\psi}}_{\mathrm{I}}, \cdot] - \boldsymbol{\mathcal{T}}_{\mathrm{I,D,I}}[\underline{\ddot{\psi}}_{\mathrm{I}}, \underline{\dot{\psi}}_{\mathrm{D}}, \cdot] \\[4pt] -\boldsymbol{\mathcal{T}}_{\mathrm{D,I,I}}[\underline{\ddot{\psi}}_{\mathrm{D}}, \underline{\dot{\psi}}_{\mathrm{I}}, \cdot] - \underline{\mathbf{A}}_{\mathrm{I}}(\underline{\psi}, \underline{\dot{\psi}}, \theta(\psi)) = F(t) \qquad\qquad \text{in } (0,T), \\[4pt] \underline{\psi} = \underline{\psi}_t = 0 \qquad\qquad\qquad\qquad\qquad\qquad\qquad\qquad\qquad \text{at } t = 0. \end{cases}$$

The right-hand side of the equation is given by

$$F(t) = -\mathbf{M}_{\mathrm{I,D}}\underline{\ddot{\psi}}_{\mathrm{D}} - \mathbf{K}_{\mathrm{I,D}}\underline{\psi}_{\mathrm{D}} - \mathbf{C}_{\mathrm{I,D}}\underline{\dot{\psi}}_{\mathrm{D}} - \boldsymbol{\mathcal{T}}_{\mathrm{D,D,I}}[\underline{\ddot{\psi}}_{\mathrm{D}}, \underline{\dot{\psi}}_{\mathrm{D}}, \cdot].$$

The underlined quantities $\underline{\psi}, \underline{\dot{\psi}},$ and $\underline{\ddot{\psi}}$ denote the coefficient vectors of $\psi, \psi_t,$ and ψ_{tt} resulting from the spatial finite element discretization. The compact notation with index sets D and I is used to extract the respective rows and columns of matrices and vectors that belong to Dirichlet and interior degrees of freedom.

The absorbing boundary vector $\underline{\mathbf{A}}$ is formally given by

(34)
$$\underline{\mathbf{A}}(\psi_t, \theta(\psi)) = (A_i(\psi_t, \theta(\psi)))_{i \in \mathrm{DOF}(\Gamma_{\mathrm{abc}})},$$

$$A_i(\psi_t, \theta(\psi)) = \int_{\Gamma_{\mathrm{abc}}} c\sqrt{1 - \sigma k\psi_t}\,\psi_t \cos\theta(\psi)\,N_i\,\mathrm{d}S.$$

Above, N_i stands for the finite element ansatz function of the i-th global degree of freedom, while $\mathrm{DOF}(\Gamma_{\mathrm{abc}})$ is the set of degrees of freedom belonging to the absorbing boundary.

The nonlinearity tensor $\boldsymbol{\mathcal{T}}$ is used to resolve the nonlinear bulk term in the weak formulation in a fixed-point iteration. The same also holds for the absorbing boundary vector which is iteratively updated with the current values of ψ_t, ψ_{tt} as well as updates for the angle θ.

The system (33) is a nonlinear system of ordinary differential equations of second order with $|\mathrm{I}|$ components. It remains to solve it by using a suitable time integrator. Following [43], we employ the Generalized-α scheme in combination with the Newmark relations for time integration. Values of the Generalized-α parameters (α_m, α_f) and the Newmark parameters $(\beta_{\mathrm{nm}}, \gamma_{\mathrm{nm}})$ that are used in experiments are chosen according to the stability and accuracy criteria stated in [4]:

$$\alpha_m = \frac{2\rho_\infty - 1}{1 + \rho_\infty}, \ \ \alpha_f = \frac{\rho_\infty}{1 + \rho_\infty}, \ \ \beta_{\mathrm{nm}} = \frac{1}{(1 + \rho_\infty)^2}, \ \ \gamma_{\mathrm{nm}} = \frac{1}{2}\frac{3 - \rho_\infty}{1 + \rho_\infty}$$

where we take $\rho_\infty = 1/2$; see also Table 1 for the resulting values.

In comparison to the numerical solvers proposed in [10, 43], a new aspect of our method is the computation of the angle of incidence $\theta(\psi)$. The angle is computed once in every time step before the first assembly of the absorbing boundary vector. Details on how we compute the angle can be found in Section 5.

TABLE 1. Time stepping parameters

	parameter	value
Newmark-parameters	β_{nm}	4/9
	γ_{nm}	5/6
Generalized-α parameters	α_m	0
	α_f	1/3
Nonlinear iteration parameters	TOL	10^{-6}
	κ_{max}	100

5. COMPUTATION OF THE ANGLE OF INCIDENCE

It remains to see how we can compute the angle of incidence θ that the local wave vector encloses with the outward normal to the absorbing boundary at a given point on Γ_{abc}. To reduce the computational cost, we compute the angle θ once per time step and do not update it within the nonlinear fixed-point iteration.

According to [51, 65], the Poynting vector $\mathbf{P}(\psi)$ of a wave field ψ can be used to compute its local propagation direction. The vector $\mathbf{P}(\psi)$ is given by

$$\mathbf{P}(\psi) = -\frac{\partial \psi}{\partial t} \nabla \psi. \tag{35}$$

Since neither the sign nor the norm of the propagation vector plays a role when computing the incidence angle, we restrict ourselves to the spatial gradient alone to determine the main propagation direction of the wave. Such an approach was also taken in [26, 64, 67] for wave fields in an isotropic medium. In our case, this method of computing the local propagation direction works especially well since, although globally discontinuous, the element-wise gradient information is readily available at every time step in the finite element framework. We also refer to [48] for a further discussion on the use of the Poynting vector in angle decomposition methods.

We conduct experiments with zero initial data and Dirichlet conditions on part of the boundary, and so most of the potential field is at rest at the beginning of the simulation. However, numerical noise of low magnitude can be present at the absorbing boundary before the wave reaches it. Such behavior could be accounted to weak ill-posedness; see [44]. To tackle this issue, we implement a switch. When going over all elements adjacent to the absorbing boundary, we only compute the element-wise angle of incidence once the local wave amplitude (in terms of absolute value of the elements degrees of freedom) exceeds a certain percentage p_1 of a reference value; see Algorithm 1, line 3. We take the reference value to be the source amplitude of the wave. In the case that the source amplitude is not known a priori, an alternative would be to compute the maximum field amplitude in the interior of the domain and take this as a reference value. As long as the criterion is not matched, the local angle of incidence is set to 0; see Algorithm 1, line 14. We note that a similar approach was taken in [54]. In all our numerical experiments, we set $p_1 = 0.1$.

Algorithm 1 summarizes our method of computing the incidence angle. Within the algorithm, indices in the exponent indicate the time step.

Algorithm 1: Angle-computation algorithm

Initialization:

1 Formally **set** $|\nabla\psi_{\text{el}}^{(-1)}| = \infty$ and $\theta_{\text{el}}^0 = 0\,^\circ$ for all elements el

In time step $n = 1, 2, ...$ **do**

2 **for** el $\in$ {**elements** : **element has an edge/face on the absorbing boundary**}

3   **if** $\max\{|\psi_i^n| : \text{dof}_i \text{ belongs to el}\} > p_1 \cdot \mathfrak{A}$ **then**

4   enable angle computation for el

5   **end**

6   **if** angle computation is enabled for el **then**

7   Evaluate $\nabla\psi(\vec{x}, t^{n-1})$ within el $\rightarrow$ save as $\nabla\psi_{\text{el}}^{n-1}$

8   **if** $|\nabla\psi_{\text{el}}^{n-1}| \leq p_2 \max\limits_{k < n-1} |\nabla\psi_{\text{el}}^k|$ **then**

9   set $\theta_{\text{el}}^n = \theta_{\text{el}}^{n-1}$

10   **else**

11   **compute** $\theta_{\text{el}}^n = \arccos\left(\dfrac{|\langle \nabla\psi_{\text{el}}^{n-1}, \vec{n}_{\text{el}}\rangle|}{|\nabla\psi_{\text{el}}^{n-1}|} \right)$

12   **end**

13   **else**

14   set $\theta_{\text{el}}^n = 0\,^\circ$

15   **end**

16 **end**

Note that even once the local amplitude of the wave at a given element is large enough for the angle computation to start, unreliable angle values can be computed at points where a local wave maximum or minimum hits the boundary since the gradient is close to zero. As a remedy, we propose that gradients with the Euclidean norm below some threshold should not influence the angle of incidence. Whenever such a small gradient appears, we use the angle of the last time step; see Algorithm 1, line 9. We employ a percentage p_2 of a reference value for the threshold. As the reference value we take the local gradient history of the given element and pick the norm-wise maximum over the past time steps; see Algorithm 1, line 8. We compute a new angle of incidence only in cases where the threshold is surpassed, i.e., when the local gradient is sufficiently large; cf. Algorithm 1, line 11. To also reduce the oscillations with respect to time in the angle distribution, in all experiments we choose a relatively high threshold of $p_2 = 0.5$.

Together with the previously introduced switch, the above approach allows steering the sensitivity of the angle computation algorithm by adapting the parameters p_1 and p_2. If these parameters are close to 1, the angle is only computed for very high amplitudes and local gradients, while for most other parts of the boundary the angle remains zero. On the other hand, small values of p_1 and p_2 lead to highly sensitive angles reacting to even small perturbations in the wave field.

6. NUMERICAL RESULTS

We proceed with numerical simulations where we put our self-adaptive technique to the test. Computational domains Ω used in numerical experiments are sketched in Figure 2. The dashed lines symbolize the boundaries of the reference domain Ω_{ref} where we compute the reference solution ψ^{ref}. The reference solution is always first computed on Ω_{ref}, then restricted to the actual domain Ω, and compared with the potential field obtained on Ω by employing the absorbing conditions.

We mention again that in all numerical simulations conforming finite elements of lowest order on simplicial meshes are used. Geometry and mesh are generated by using the Gmsh software package [11].
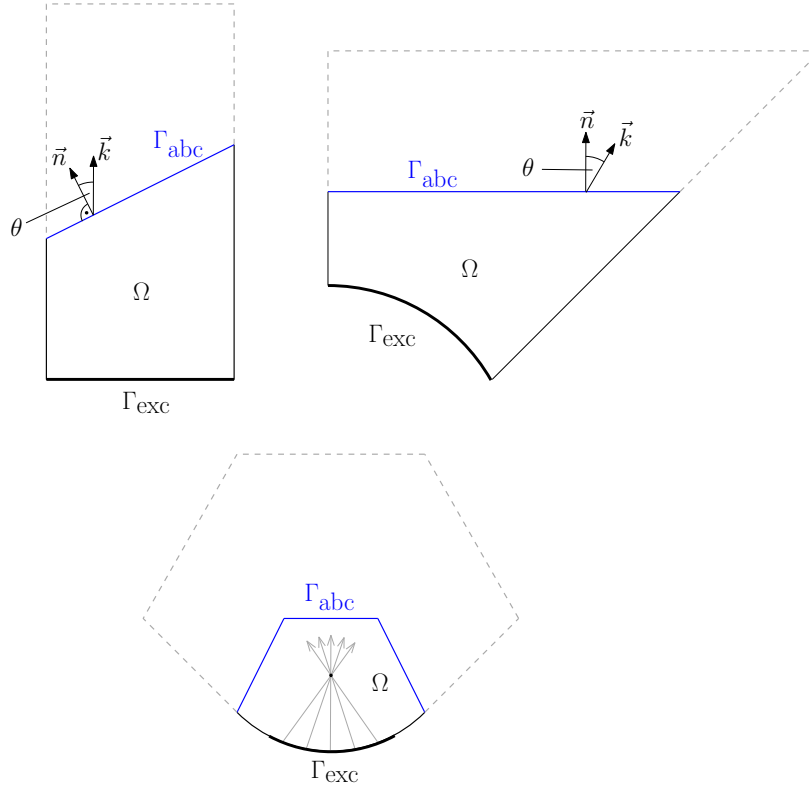

FIGURE 2. Computational domains used in simulations. **(Top left)** Channel with an inclined absorbing boundary, **(Top right)** Octant of a "plate with hole" geometry, **(Bottom)** Geometry of a focusing transducer.

6.1. **Domain with an inclined absorbing boundary.** In our first experiment, we consider a two-dimensional channel geometry, where the upper (absorbing) boundary Γ_{abc} is tilted by a given angle of θ; see Figure 2. The waves originate from the excitation boundary Γ_{exc} at the bottom of the rectangle and travel straight upwards. We impose homogeneous Neumann boundary conditions on the sides of the domain. The wave vector $\vec{k}$ in this setting points straight upwards. Therefore, the angle that the wave vector and the outward normal $\vec{n}$ of Ω at Γ_{abc} enclose is exactly θ for the absorbing boundary.

We compute the reference solution ψ^{ref} on a larger domain without the absorbing boundary and then conduct a simulation on Ω. To get an impression on how the wave propagates in the present setting, Figure 3 shows the potential field ψ at different time snapshots. Material parameters were chosen to be the ones of water, i.e.

$$c = 1500\,\mathrm{m/s},\ b = 6 \cdot 10^{-9}\,\mathrm{m^2/s},\ \rho = 1000\,\mathrm{kg/m^3},\ B/A = 5;$$

see [33, Chapter 5], while the excitation (31) has an amplitude of $\mathfrak{A} = 0.01\,\mathrm{m^2/s^2}$ and a frequency of $210\,\mathrm{kHz}$. The experiment was conducted for two different angles

$$\theta \in \{20°, 50°\}.$$

For spatial discretization, we take 13045 ($20°$ case) and 13046 ($50°$ case) degrees of freedom in space for the channel width of $0.02\,\mathrm{m}$ and channel length (in the middle) of $0.03\,\mathrm{m}$. In time, 9800 time steps were taken to cover the interval from $t_0 = 0$ until $T = 9.45 \cdot 10^{-5}\,\mathrm{s}$.

The error plots are given in Figure 4. We observe that the conditions that do not take the angle of incidence into consideration significantly deteriorate when the angle increases. For the angle of incidence $\theta = 50°$, the maximal relative error is more than 20% for the linear conditions and around 17% for the nonlinear conditions with the fixed angle $\theta = 0°$. In comparison, the self-adaptive technique when combined with the nonlinear conditions (26) allows for the error to remain around 1%. Note that linearization (10) and the resulting absorbing conditions (26) clearly outperform conditions (28). We, therefore, proceed in the following experiments with testing only (26) in combination with the self-adaptive technique. We also observe that the nonlinear conditions (26) that use an approximate angle computation via the gradient of the wave field perform similarly to the conditions that employ the exact angle.
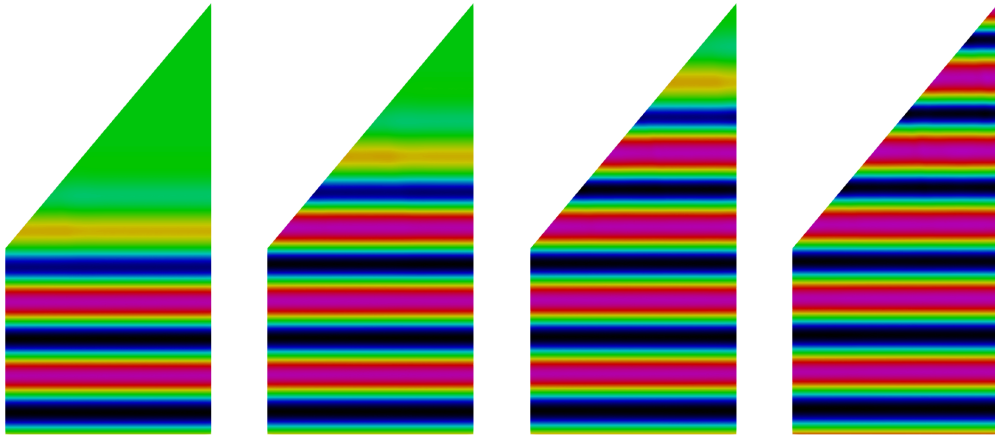
FIGURE 3. Time-snapshots of the potential field.
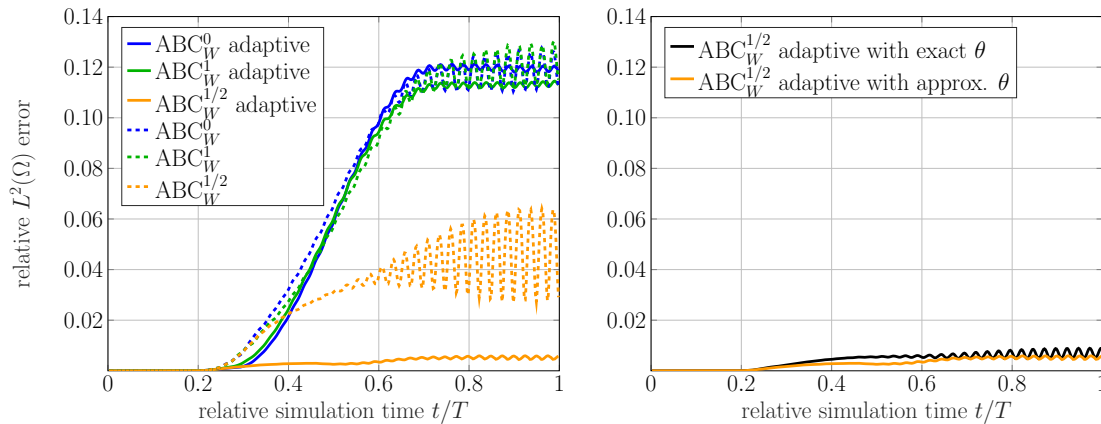
FIGURE 4. **Inclined plane boundary:** Relative $L^2(\Omega)$ error of the potential $\psi(t)$ over the simulation time with $\theta = 20°$. **(Left)** Nonlinear vs. linear conditions with and without adaptivity, **(Right)** Performance of adaptive conditions with numerically computed vs. the exact incidence angle θ.

It is also interesting to see how the errors are distributed over the domain Ω, i.e., where they originate from and how far they spread. Figure 6 shows the error fields $|\psi(t) - \psi^{\mathrm{ref}}(t)|$ at different

times for the $\text{ABC}_W^{1/2}$ conditions with and without adaptivity. The first snapshots were taken just as the first wave hits the absorbing boundary. In the subsequent snapshots, we can see how the erroneous reflections travel together with the wave across the absorbing boundary. It is evident that there are fewer reflections present when using the self-adaptive absorbing boundary conditions that take the local angle information into account.
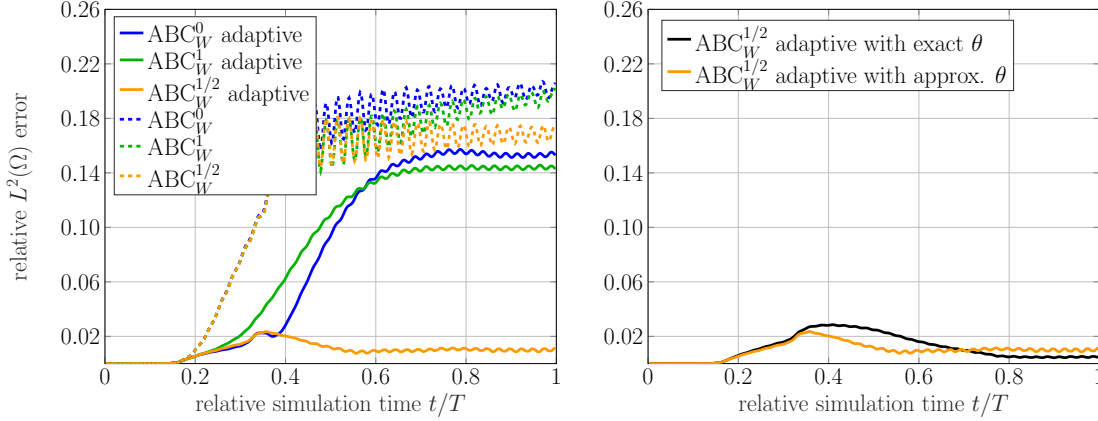

FIGURE 5. **Inclined plane boundary:** Relative $L^2(\Omega)$ error of the potential $\psi(t)$ over the simulation time with $\theta = 50°$. **(Left)** Nonlinear vs. linear conditions with and without adaptivity, **(Right)** Performance of adaptive conditions with numerically computed vs. the exact incidence angle θ.

6.2. **Higher source frequency.** So far our experiments have been conducted with the same source excitation. After varying the domain geometry via the angle θ, we investigate the influence of the source frequency on the quality of absorbing conditions. We now test with the excitation frequency

$$f = 250\,\text{kHz}.$$

All the remaining parameters being the same as before. The domain again has the upper boundary tilted with the angle of $50°$. Figure 7 shows the error plots for the higher frequency. We observe that conditions ABC_W^0 asymptotically show the same poor results as conditions ABC_W^0 with self-adaptivity. Only our combination of nonlinear conditions with the self-adaptive technique (26) allows for the relative error to stay around 1 %. By comparing Figure 5 and Figure 7, we also notice that the difference in the error between the nonlinear and the corresponding linear conditions increases with the frequency, emphasizing the need to employ nonlinear conditions for high-frequency nonlinear sound waves.
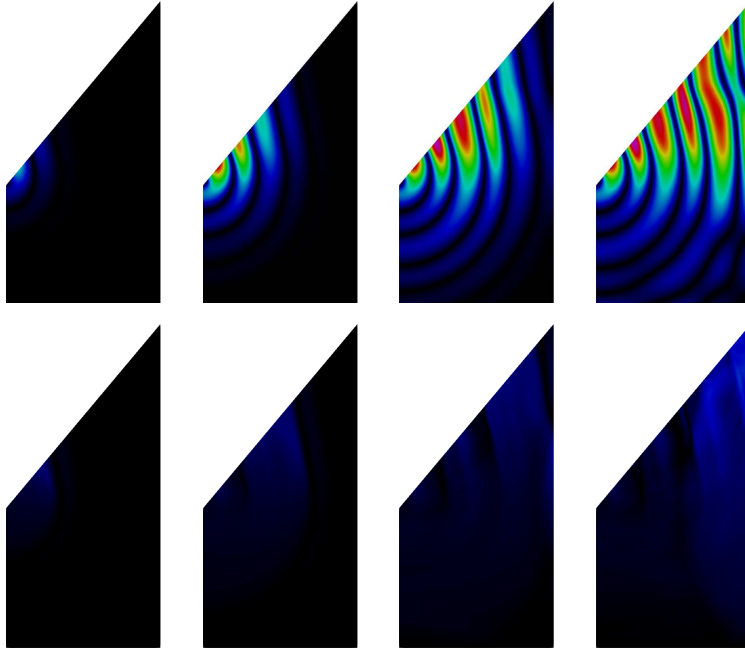
FIGURE 6. Potential Difference $|\psi(t) - \psi^{\mathrm{ref}}(t)|$ plotted over time **(Horizontal)** for $\mathrm{ABC}_W^{1/2}$ **(First row)** without adaptivity and **(Second row)** with self-adaptive angle.
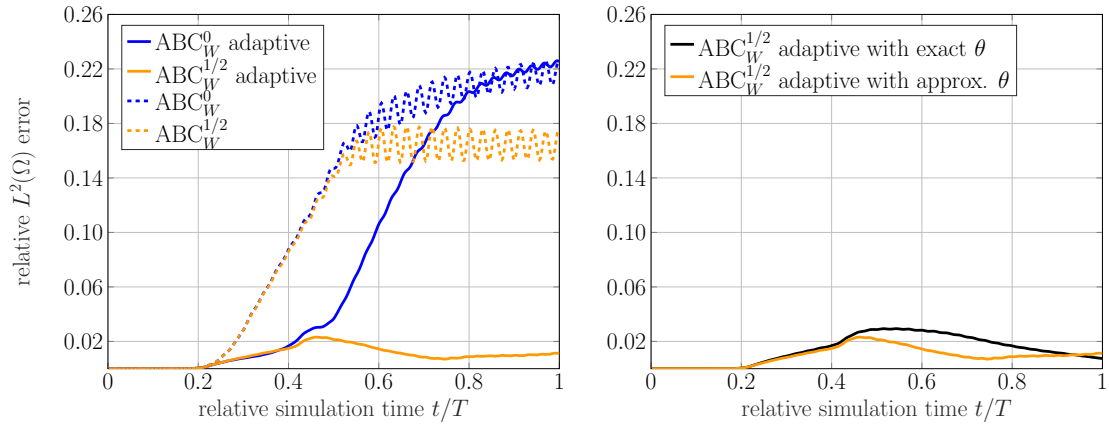

FIGURE 7. **Inclined plane boundary:** Relative $L^2(\Omega)$ error of the potential $\psi(t)$ for $t \in [0, T]$ with $\theta = 50°$ and higher source frequency. **(Left)** Nonlinear vs. linear conditions with and without adaptivity, **(Right)** Performance of adaptive conditions with numerically computed vs. the exact incidence angle θ.

6.3. **Plate with a hole.** We previously tested the new absorbing boundary conditions in a domain where the angle of incidence was constant over the absorbing boundary. To show that both our approach of computing the angle of incidence of the wave as well as the nonlinear boundary conditions work in more realistic settings, we now consider the so-called *"plate with a hole"* domain. It consists of a square with a circular hole in the center. In our case, the excitation of the wave takes place at the boundary of the hole. By using symmetry, we reduce the simulation of the whole domain to half of one of its quarters; see Figure 2.

An analytical expression for the angle of incidence is also available here which allows us to judge the quality of our angle approximation. If the origin is at the center of the circular hole and the square has sides of length a, the angle of incidence is given by

$$(36) \qquad \theta(x, y, t) = \arccos\left(\frac{a/2}{\sqrt{x^2 + (a/2)^2}}\right).$$

We set $a = 0.08$ in the experiments. The domain is resolved with 13820 degrees of freedom in space. For time discretization, we choose 8330 time steps with final time $T = 8.0325 \cdot 10^{-5}\,$s.

Figure 8 shows the angle of incidence computed by our approach at two different points in time and further illustrates our criterion on computing the incidence angle based on the amplitude of the wave on the boundary. Note that formula (36) assumes a reflection-free potential field so an exact match of our angle to the analytical angle distribution cannot be expected. In fact, our method tries to compensate also for the waves that originate as spurious reflections from the absorbing boundary.
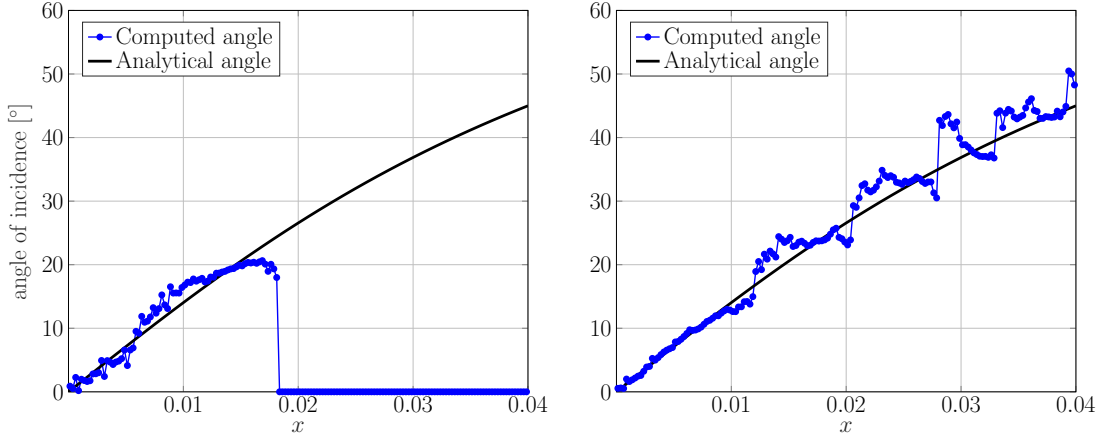

FIGURE 8. Computed versus exact angle of incidence θ. **(Left)** The angle is only computed on the parts of the absorbing boundary that the wave has reached. **(Right)** Angle computation towards the end of the simulation.

As in our last experiment, we proceed by showing the wave field at different time steps as well as the error comparison of different absorbing boundary conditions; see Figure 9 and Figure 11. This time we also compute them in terms of the acoustic pressure $u = \rho\psi_t$ due to its practical importance. We also introduce here the relative errors in the $L^2(0, T; L^2(\Omega))$ norm, i.e.

$$e_\psi = \frac{\|\psi - \psi^{\mathrm{ref}}\|_{L^2(0,T;L^2(\Omega))}}{\|\psi^{\mathrm{ref}}\|_{L^2(0,T;L^2(\Omega))}}, \qquad e_u = \frac{\|u - u^{\mathrm{ref}}\|_{L^2(0,T;L^2(\Omega))}}{\|u^{\mathrm{ref}}\|_{L^2(0,T;L^2(\Omega))}}.$$

In the present experiment, those errors amount to $e_\psi = 1.82\,\%$ and $e_u = 0.93\,\%$ for the self-adaptive conditions and $e_\psi = 5.41\,\%$ and $e_u = 5.17\,\%$ for the conditions without adaptivity, giving an overall improvement of $66.36\,\%$ in the potential and $82.01\,\%$ in the pressure.

Plots of the difference field $|u(t) - u^{\text{ref}}(t)|$ at different times are given in Figure 10. We observe that with the absorbing conditions that are not adaptive, the amplitude of the error increases over the width of the domain as the angle grows.
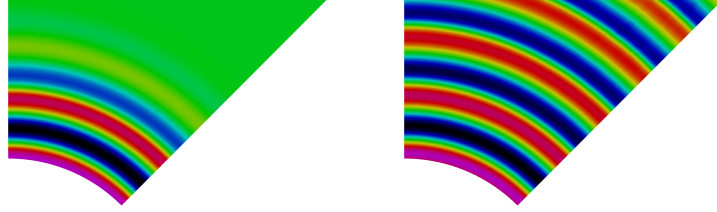

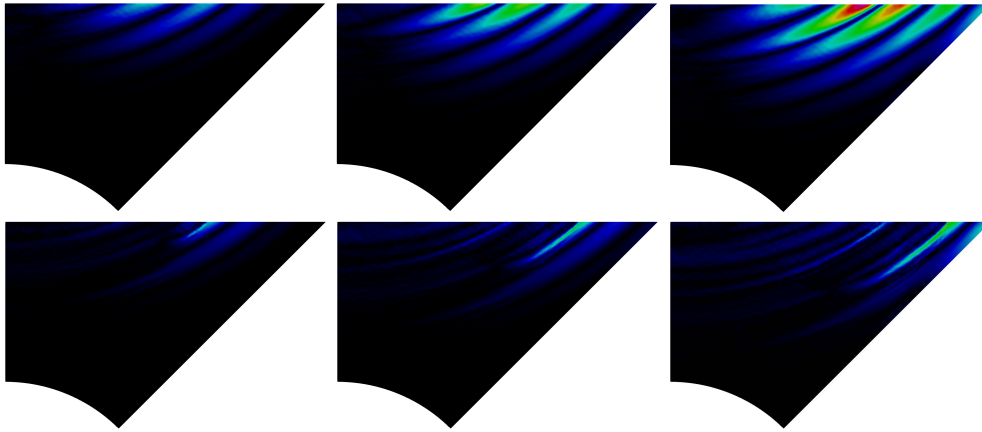FIGURE 9. Time snapshots of the pressure field $u = \rho \psi_t$.

FIGURE 10. Pressure difference $|u(t) - u^{\text{ref}}(t)|$ plotted over time **(Horizontal)** for $\text{ABC}_W^{1/2}$ without **(First row)** and with **(Second row)** angle consideration.
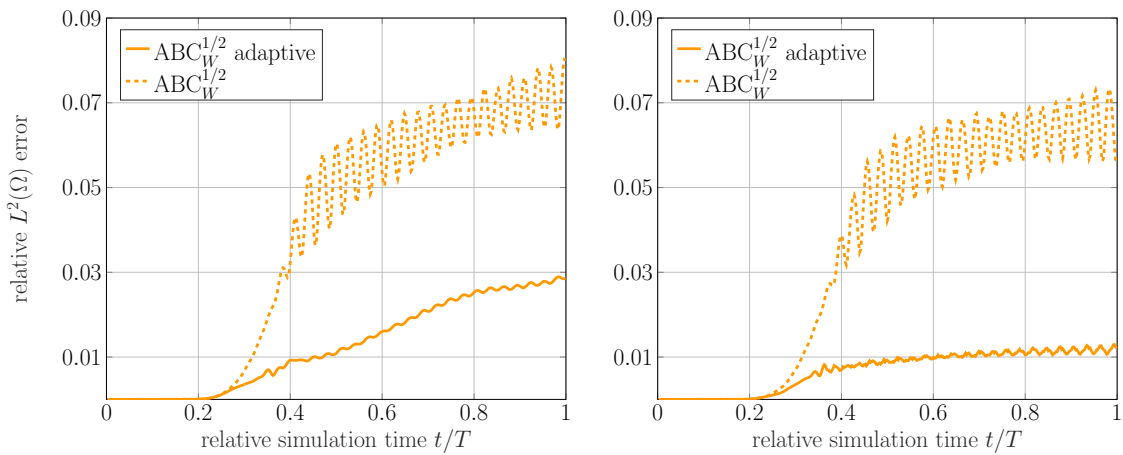
FIGURE 11. **Plate with a hole:** Relative $L^2(\Omega)$ error of **(Left)** the potential $\psi(t)$ and **(Right)** the pressure $u(t) = \rho \psi_t(t)$ over the simulation time.

6.4. **High-intensity focused ultrasound (HIFU).** We next simulate the potential field generated by a piezoelectric transducer. Such devices are made of small plates of a piezoelectric material that are aligned in an arc-shaped array pointing towards a common focal point [6, 59]. When set into motion, those vibrating plates induce acoustic sound waves that propagate towards the focal point. As it travels, the wave is focused more and more the closer it comes to the focal point. This technique of generating high-pressure amplitudes at specific locations is used in medicine to treat kidney stones and certain types of cancer; see [24, 35, 36, 62, 66]. The pressure levels in the non-focal region are sufficiently low so that damage to the surrounding tissue is avoided.

For this experiment, the medium of propagation is again chosen to be water with the same physical parameters as before. The source frequency is again given by $f = 210 \, \text{kHz}$ and the source amplitude by $\mathcal{A} = 0.02 \, \text{m}^2/\text{s}^2$ which increases at the focal point due to focusing. As depicted in Figure 2, the absorbing boundary here consists out of three line segments at the left, right and top. Time-snapshots of the transducer simulation can be seen in Figure 12.

The computational domain was resolved with 13313 degrees of freedom, while for the time stepping 9800 steps and a final time of $T = 4.725 \cdot 10^{-5} \, \text{s}$ were used.
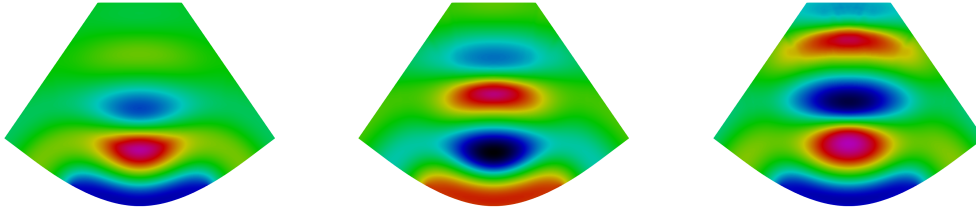

FIGURE 12. Snapshots of the pressure field $u = \rho \psi_t$ of a propagating, self-focusing wave.

A comparison of the relative $L^2(\Omega)$ errors at every time step is displayed in Figure 13. Due to the relevance of measuring the acoustic pressure in HIFU applications, we again also plot the relative error that the absorbing boundary conditions produce in the pressure $u = \rho \psi_t$. We observe that the qualitative behavior of the errors and especially also the improvement made by the new adaptive conditions remains the same. For the adaptive conditions, the relative errors in the $L^2(0, T; L^2(\Omega))$ norm are $e_\psi = 4.12 \, \%$ and $e_u = 4.46 \, \%$, whereas $e_\psi = 7.94 \, \%$ and $e_u = 7.27 \, \%$ if the adaptivity is not considered, resulting in an improvement of $51.89 \, \%$ in ψ and even $61.35 \, \%$ in u. The increase in computational time when using the adaptive absorbing conditions amounts to $1.5 \, \%$.
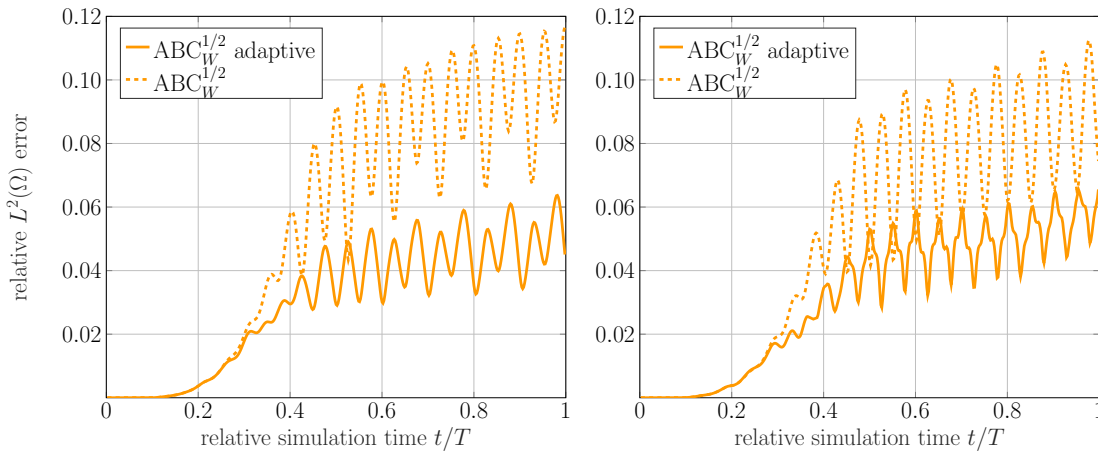

FIGURE 13. **HIFU transducer in 2D:** Relative $L^2(\Omega)$ error of **(Left)** the potential $\psi(t)$ and **(Right)** the pressure $u(t) = \rho \psi_t(t)$ over the simulation time.

Since even with the absorbing boundary conditions an impinging wave is not completely absorbed, there are always some spurious reflections that travel back into the interior of the domain. They then interact with the "main" wave that still travels towards the boundary and other spurious reflections originating from different parts of the boundary. Those effects together can accumulate over time, leading to an increase of the deviation from the reference solution and therefore the error, as can be observed in Figure 13. These effects appear to be more pronounced in more complicated geometries as well as with wave focusing.

6.5. **Multi-source wave superposition.** Our next experiment is intended to illustrate that the adaptive method also works in scenarios with more than one wave source present and when superposition of waves occurs. In such cases, we can expect a less distinct wave propagation direction. In contrast to the other examples, here we use a source term on the right-hand side of the Westervelt equation. The computational domain is given by the square $\Omega = (0, 0.03)^2$ and we choose the source term as follows

$$
f(x, y, t) = \mathfrak{A} \sin(\omega t) \left[\exp \left(- \left(\frac{x - x_{\mathrm{mp1}}}{\sigma_x} \right)^2 - \left(\frac{y - y_{\mathrm{mp1}}}{\sigma_y} \right)^2 \right) \right.
$$
$$
\left. - \frac{2}{3} \exp \left(- \left(\frac{x - x_{\mathrm{mp2}}}{\sigma_x} \right)^2 - \left(\frac{y - y_{\mathrm{mp2}}}{\sigma_y} \right)^2 \right) \right],
$$

with $\sigma_x = \sigma_y = 0.0005$, $x_{\mathrm{mp1}} = 0.02, x_{\mathrm{mp2}} = 0.01$, $y_{\mathrm{mp1}} = y_{\mathrm{mp2}} = 0.015$, and $\mathfrak{A} = 10^{11} \, \mathrm{m}^2/\mathrm{s}^4$. Figure 14 depicts wave propagation at two different time induced by two different source terms within the computational domain. The transparent region depicts the reference domain. In Figure 15, we can see the relative L^2 errors. We observe that also in this setting the adaptive approach results in a smaller error and a better overall behavior.
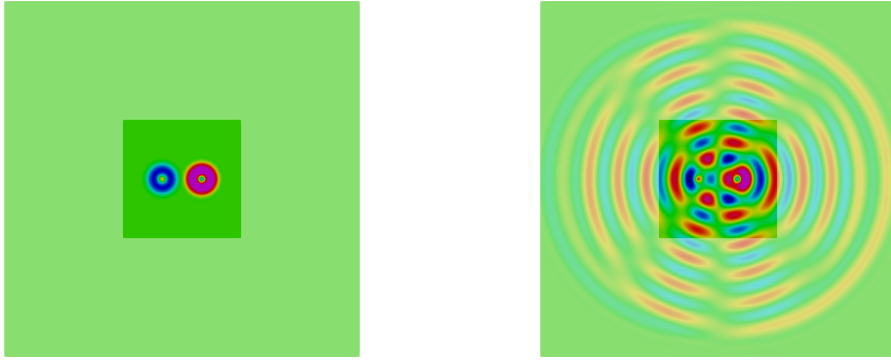

FIGURE 14. Wave propagation induced by two different source terms.

6.6. **3D Transducer.** To also show the capability of our method in three dimensions, we perform another experiment in a transducer setting, this time in 3D. Due to the high computational costs, especially for the reference solution on the larger domain Ω^{ref}, we choose a source amplitude of $\mathfrak{A} = 0.002 \, \mathrm{m}^2/\mathrm{s}^2$, while keeping physical parameters and the excitation frequency the same. Figure 16 shows the computational domain together with the grid, while Figure 17 depicts the three-dimensional wave propagation in the given domain.

In Figure 18, we compare the adaptive conditions to the nonlinear conditions with the fixed angle $\theta = 0\,^\circ$.

Note that in 3D, in addition to the discretization error, there is also an interpolation error caused by a mismatch between the grid for the simulation with absorbing conditions and the mesh of the reference solution. Combined with the L^2-norm of the reference solution being small at the beginning
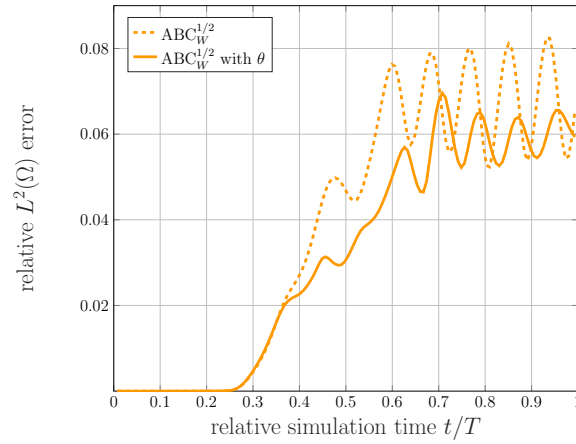
FIGURE 15. **Multi-source wave superposition:** Relative $L^2(\Omega)$ error of the potential $\psi(t)$
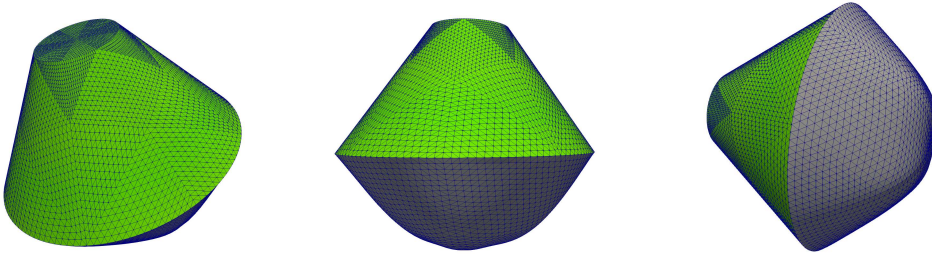

FIGURE 16. Three-dimensional transducer geometry with mesh visible on the surface. Absorbing conditions are employed on the green surface, Dirichlet conditions on the grey.

of the simulation, this results in the initial peak in the relative error for both adaptive and non-adaptive conditions. In 2D, the meshing software was able to avoid the interpolation error. In the long term behavior as well as in the absolute errors, we observe that the adaptive angle information improves the quality of the conditions. The qualitative behavior of the errors of the new adaptive conditions is similar in 3D. The relative errors in the $L^2(0,T;L^2(\Omega))$ norm are $e_\psi = 8.28\,\%$ and $e_u = 8.3\,\%$ if the adaptivity is considered, whereas $e_\psi = 10.34\,\%$ and $e_u = 10.39\,\%$ if the adaptivity is not considered, resulting in an improvement of $19.92\,\%$ in ψ and $20.12\,\%$ in u.
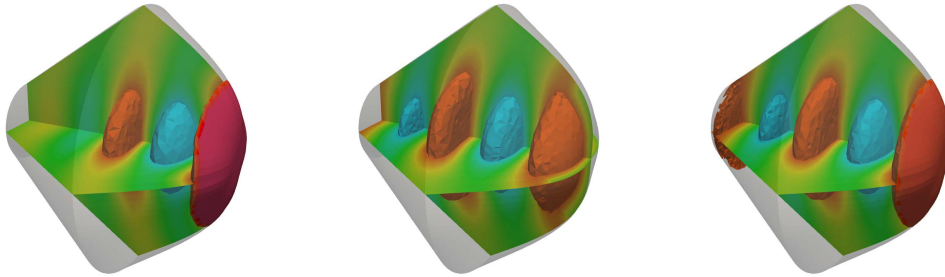
FIGURE 17. Three-dimensional propagation of the pressure wave $u = \rho\psi_t$. The iso-volumes show the regions of highest (in absolute value) pressure amplitudes in 3D, while the two planes show slices through the three-dimensional pressure field.
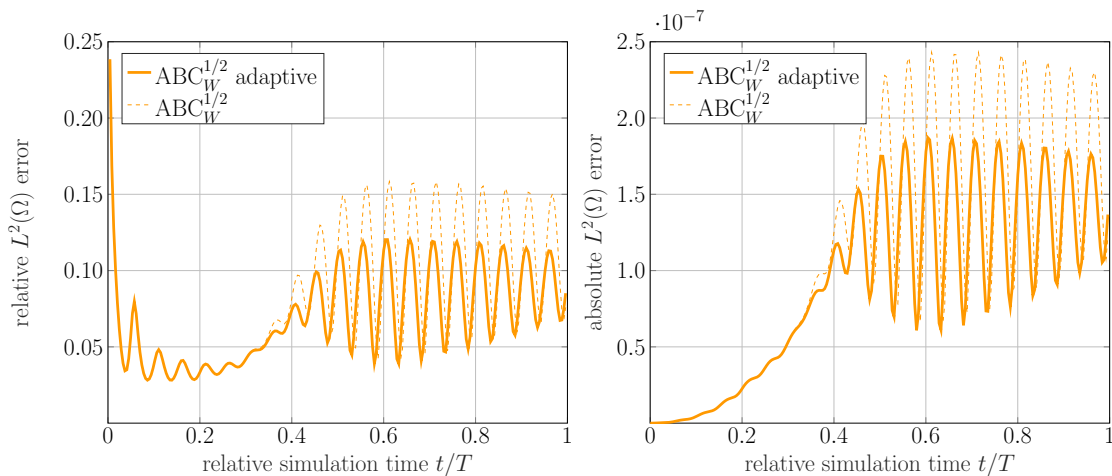

FIGURE 18. **HIFU transducer 3D: (Left)** Relative $L^2(\Omega)$ error of the potential $\psi(t)$, **(Right)** Absolute $L^2(\Omega)$ error of the potential $\psi(t)$.

6.7. **3D Acoustic horn.** Nonlinear sound propagation has been widely reported to occur in wind instruments; see [3, 9, 45, 50]. Motivated by this, for our final experiment, we consider a numerical simulation of an acoustic horn.

The excitation takes place at the bottom of the domain and the waves then travel through a waveguide with an increasing diameter; see Figure 20. At the end of the waveguide, where the wave starts to propagate into the ambient space, we employ again the absorbing conditions to truncate the domain at a spherical boundary. In this experiment we use the physical parameters of air instead of water:

$$c = 331\,\frac{\text{m}}{\text{s}},\ b = 0.00005\,\frac{\text{kg}}{\text{m s}},\ B/A = 1.2,\ \varrho = 1.29\,\frac{\text{kg}}{\text{m}^3};$$

see [14]. The excitation has a frequency of $f = 6.5\,\text{kHz}$ and an amplitude of $\mathfrak{A} = 0.01\,\text{m}^2/\text{s}^2$. To keep the computational cost reasonable, we again use symmetry to reduce the simulation to a quarter of the actual three-dimensional acoustic horn. The two planes of symmetry are equipped with homogeneous Neumann conditions; see Figure 19. A comparison of adaptive and non-adaptive conditions is given in Figure 21. The relative errors in the $L^2(0, T; L^2(\Omega))$ norm are $e_\psi = 5.23\,\%$ and $e_u = 5.33\,\%$ if the adaptivity is considered, whereas $e_\psi = 6.11\,\%$ and $e_u = 6.07\,\%$ if the adaptivity is not considered, resulting in an improvement of $14.4\,\%$ in ψ and $12.19\,\%$ in u.
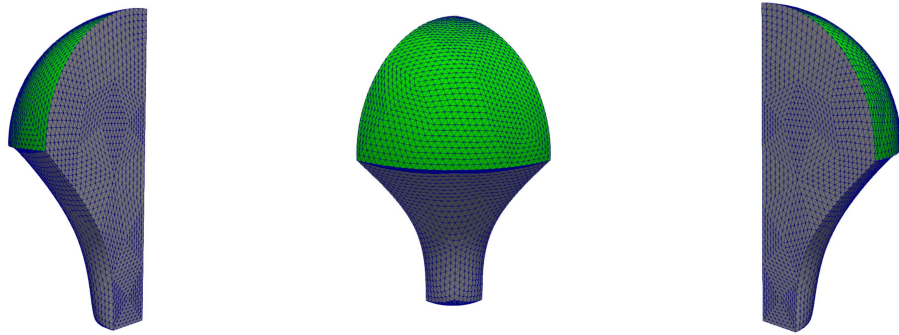
FIGURE 19. Three-dimensional acoustic horn geometry with mesh visible on the surface. Absorbing conditions are employed on the green surface, homogeneous Neumann conditions on the grey and a wave excitation via inhomogeneous Dirichlet conditions at the bottom surface.
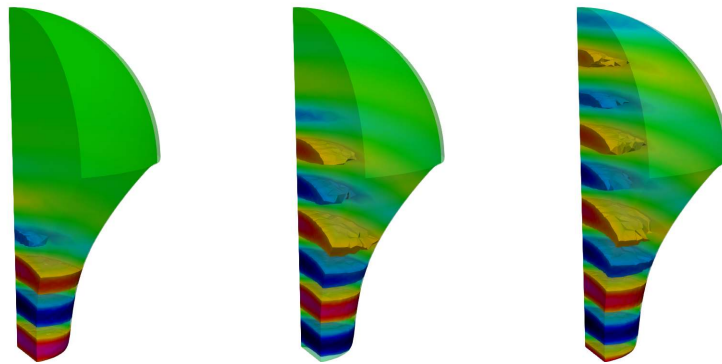

FIGURE 20. Three-dimensional propagation of the pressure wave $u = \rho\psi_t$. The isovolumes show the regions of highest (in absolute value) pressure amplitudes in 3D.

We observe less of a gain in our recent examples compared to the introductory ones in 2D, which has a natural explanation. In our simplest 2D setting in Section 6.1, the angle of incidence is constant over the whole absorbing boundary and large, so the boundary conditions can significantly profit from taking the angle information into account adaptively. In the later, more advanced examples (e.g., in Section 6.3) a large portion of the wave leaves the domain with quite small incidence angles. The same also holds for the application-oriented example of the focusing transducer in Sections 6.4 and 6.6. There, most of the angles of incidence are smaller than in the introductory examples which results smaller improvement compared to the standard non-adaptive conditions.

7. Conclusion

We have developed a self-adaptive absorbing technique for sound propagation in the presence of nonlinearities. Within our approach, the angle of incidence of the wave is computed locally by employing the information given by the gradient of the wave field. The absorbing conditions are then updated in real time with the angle values.

The method offers three fundamental advantages. It is sufficiently accurate over a range of angles of incidence, and it is easy to implement. Moreover, by only relying on the gradient of the wave field
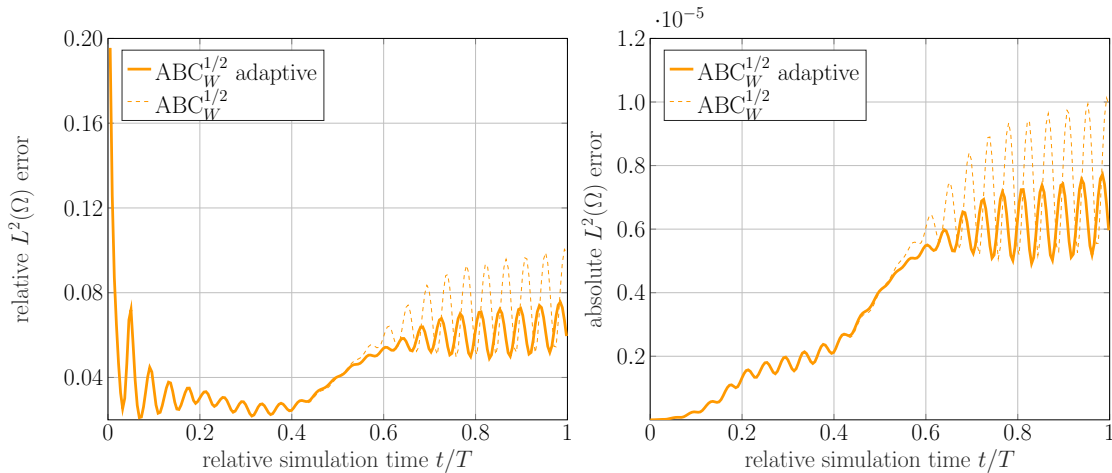
FIGURE 21. **Acoustic horn 3D: (Left)** Relative $L^2(\Omega)$ error of the potential $\psi(t)$, **(Right)** Absolute $L^2(\Omega)$ error of the potential $\psi(t)$ over the simulation time.

which is readily available in finite element simulations, we can keep the additional computational efforts low.

References

[1] S. Abarbanel, D. Gottlieb, and J. S. Hesthaven, *Well-posed perfectly matched layers for advective acoustics*, Journal of Computational Physics, 154 (1999), pp. 266–283.

[2] J.-P. Bérenger, *A perfectly matched layer for the absorption of electromagnetic waves*, Journal of Computational Physics, 114 (1994), pp. 185–200.

[3] H. Berjamin, B. Lombard, C. Vergez, and E. Cottanceau, *Time-domain numerical modeling of brass instruments including nonlinear wave propagation, viscothermal losses, and lips vibration*, Acta Acustica united with Acustica, 103 (2017), pp. 117–131.

[4] A. Bonelli, O. Bursi, S. Erlicher, and L. Vulcan, *Analysis of the Generalized-α method for linear and non-linear forced excited systems*, in Structural Dynamics-EURODYN, vol. 2, Citeseer, (2002), pp. 1523–1528.

[5] D. G. Crighton, *Model equations of nonlinear acoustics*, Annual Review of Fluid Mechanics, 11 (1979), pp. 11–33.

[6] T. Dreyer, W. Krauss, E. Bauer, and R. Riedlinger, *Investigations of compact self focusing transducers using stacked piezoelectric elements for strong sound pulses in therapy*, in Ultrasonics Symposium, 2000 IEEE, vol. 2, IEEE, 2000, pp. 1239–1242.

[7] B. Engquist and A. Majda, *Absorbing boundary conditions for the numerical simulation of waves*, Proceedings of the National Academy of Sciences, 74 (1977), pp. 1765–1766.

[8] G. M. Fierro, F. Ciampa, D. Ginzburg, E. Onder, and M. Meo, *Nonlinear ultrasound modelling and validation of fatigue damage*, Journal of Sound and Vibration, 343 (2015), pp. 121–130.

[9] N. Fletcher, *Nonlinear theory of musical wind instruments*, Applied Acoustics, 30 (1990), pp. 85–115.

[10] M. Fritz, V. Nikolić, and B. Wohlmuth, *Well-posedness and numerical treatment of the Blackstock equation in nonlinear acoustics*, Mathematical Models and Methods in the Applied Sciences M3AS, 28 (2018), pp. 2557–2597.

[11] C. Geuzaine and J.-F. Remacle, *Gmsh: A three-dimensional finite element mesh generator with built-in pre- and post-processing facilities*, International Journal for Numerical Methods in Engineering, 79(11) (2009), pp. 1309–1331.

[12] D. Givoli, *Non-reflecting boundary conditions*, Journal of Computational Physics, 94 (1991), pp. 1–29.

[13] D. Gordon, R. Gordon, and E. Turkel, *Compact high order schemes with gradient-direction derivatives for absorbing boundary conditions*, Journal of Computational Physics, 297 (2015), pp. 295–315.

[14] T. Gudra and K. Opieliński, *The parametric formation of acoustic waves in the air by using ultrasonic transducers*, Revista de Acustica XXXII, Sevilla, (2002).

[15] M. F. Hamilton and D. T. Blackstock, *Nonlinear acoustics*, vol. 1, Academic press San Diego, 1998.

[16] G. HEDSTROM, *Nonreflecting boundary conditions for nonlinear hyperbolic systems*, Journal of Computational Physics, 30 (1979), pp. 222–237.

[17] S. HEIN, T. HOHAGE, W. KOCH, AND J. SCHÖBERL, *Acoustic resonances in a high-lift configuration*, Journal of Fluid Mechanics, 582 (2007), pp. 179–202.

[18] J. S. HESTHAVEN, *On the analysis and construction of perfectly matched layers for the linearized Euler equations*, Journal of Computational Physics, 142 (1998), pp. 129–147.

[19] R. L. HIGDON, *Absorbing boundary conditions for difference approximations to the multidimensional wave equation*, Mathematics of Computation, 47 (1986), pp. 437–459.

[20] ———, *Numerical absorbing boundary conditions for the wave equation*, Mathematics of Computation, 49 (1987), pp. 65–90.

[21] J. HOFFELNER, H. LANDES, M. KALTENBACHER, AND R. LERCH, *Finite element simulation of nonlinear wave propagation in thermoviscous fluids including dissipation*, IEEE transactions on ultrasonics, ferroelectrics, and frequency control, 48 (2001), pp. 779–786.

[22] L. HÖRMANDER, *Pseudo-differential operators*, Communications on Pure and Applied Mathematics, 18 (1965), pp. 501–517.

[23] ———, *The analysis of linear partial differential operators III: Pseudo-differential operators*, vol. 274, Springer Science & Business Media, 1994.

[24] R. ILLING, J. KENNEDY, F. WU, G. TER HAAR, A. PROTHEROE, P. FRIEND, F. GLEESON, D. CRANSTON, R. PHILLIPS, AND M. MIDDLETON, *The safety and feasibility of extracorporeal high-intensity focused ultrasound (HIFU) for the treatment of liver and kidney tumours in a western population*, British Journal of Cancer, 93 (2005), p. 890.

[25] K.-Y. JHANG, *Nonlinear ultrasonic techniques for nondestructive assessment of micro damage in material: a review*, International Journal of Precision Engineering and Manufacturing, 10 (2009), pp. 123–135.

[26] X. JIA AND R.-S. WU, *Calculation of the wave propagation angle in complex media: Application to turning wave simulations*, Geophysical Journal International, 178 (2009), pp. 1565–1573.

[27] J.-M. JIN AND N. LU, *Application of adaptive absorbing boundary condition to finite element solution of three-dimensional scattering*, IEE Proceedings-Microwaves, Antennas and Propagation, 143 (1996), pp. 57–61.

[28] Y. KAGAWA, T. TSUCHIYA, T. YAMABUCHI, H. KAWABE, AND T. FUJII, *Finite element simulation of non-linear sound wave propagation*, Journal of sound and vibration, 154 (1992), pp. 125–145.

[29] B. KALTENBACHER, M. KALTENBACHER, AND I. SIM, *A modified and stable version of a perfectly matched layer technique for the 3-d second order wave equation in time domain with an application to aeroacoustics*, Journal of Computational Physics, 235 (2013), pp. 407–422.

[30] B. KALTENBACHER AND I. LASIECKA, *Global existence and exponential decay rates for the Westervelt equation*, Discrete and Continuous Dynamical Systems Series S, 2 (2009), p. 503.

[31] ———, *Well-posedness of the Westervelt and the Kuznetsov equation with nonhomogeneous Neumann boundary conditions*, Discrete Contin. Dyn. Syst: Conference Publications, 2 (2011), pp. 763–773.

[32] B. KALTENBACHER AND M. THALHAMMER, *Fundamental models in nonlinear acoustics part I. Analytical comparison*, Mathematical Models and Methods in Applied Sciences, 28 (2018), pp. 2403–2455.

[33] M. KALTENBACHER, *Numerical simulation of mechatronic sensors and actuators*, vol. 2, Springer, 2007.

[34] S. KAWASHIMA AND Y. SHIBATA, *Global existence and exponential stability of small solutions to nonlinear viscoelasticity*, Communications in Mathematical Physics, 148 (1992), pp. 189–208.

[35] J. KENNEDY, F. WU, G. TER HAAR, F. GLEESON, R. PHILLIPS, M. MIDDLETON, AND D. CRANSTON, *High-intensity focused ultrasound for the treatment of liver tumours*, Ultrasonics, 42 (2004), pp. 931–935.

[36] J. E. KENNEDY, *High-intensity focused ultrasound in the treatment of solid tumours*, Nature Reviews Cancer, 5 (2005), p. 321.

[37] R. G. KEYS, *Absorbing boundary conditions for acoustic media*, Geophysics, 50 (1985), pp. 892–902.

[38] V. KUZNETSOV, *Equations of nonlinear acoustics*, Sov. Phys. Acoust., 16 (1971), pp. 467–470.

[39] H. LI, X. WU, AND J. ZHANG, *Local absorbing boundary conditions for nonlinear wave equation on unbounded domain*, Physical Review E, 84: 036707 (2011).

[40] Y. LI AND Z. J. CENDES, *Adaptive absorbing boundary conditions for high accuracy scattering*, in Antennas and Propagation Society International Symposium, 1994. AP-S. Digest, vol. 1, IEEE, 1994, pp. 402–405.

[41] A. MAJDA AND S. OSHER, *Reflection of singularities at the boundary*, Communications on Pure and Applied Mathematics, 28 (1975), pp. 479–499.

[42] K. MATLACK, J. WALL, J.-Y. KIM, J. QU, L. JACOBS, AND H.-W. VIEHRIG, *Evaluation of radiation damage using nonlinear ultrasound*, Journal of Applied Physics, 111, 054911 (2012).

[43] M. MUHR, V. NIKOLIĆ, B. WOHLMUTH, AND L. WUNDERLICH, *Isogeometric shape optimization for nonlinear ultrasound focusing*, Evolution Equations & Control Theory, 8 (2019), pp. 163–202.

[44] W. MULDER, *Experiments with Higdon's absorbing boundary conditions for a number of wave equations*, Computational Geosciences, 1 (1997), p. 85.

[45] A. MYERS, R. W. PYLE JR, J. GILBERT, D. M. CAMPBELL, J. P. CHICK, AND S. LOGIE, *Effects of nonlinear sound propagation on the characteristic timbres of brass instruments*, The Journal of the Acoustical Society of America, 131 (2012), pp. 678–688.

[46] F. Nataf, *Absorbing boundary conditions and perfectly matched layers in wave propagation problems*, in Direct and Inverse problems in Wave Propagation and Applications, vol. 14, de Gruyter, (2013), pp. 219–231.

[47] L. Nirenberg, *Lectures on linear partial differential equations*, vol. 17, American Mathematical Soc., 1973.

[48] N. Patrikeeva and P. Sava, *Comparison of angle decomposition methods for wave-equation migration*, in SEG Technical Program Expanded Abstracts 2013, Society of Exploration Geophysicists, 2013, pp. 3773–3778.

[49] Q. Qi and T. L. Geers, *Evaluation of the perfectly matched layer for computational acoustics*, Journal of Computational Physics, 139 (1998), pp. 166–183.

[50] P. L. Rendón, R. Ezeta, and A. Pérez-López, *Nonlinear sound propagation in trumpets*, Acta Acustica united with Acustica, 99 (2013), pp. 607–614.

[51] A. Richardson and A. E. Malcolm, *Separating a wavefield by propagation direction*, in SEG Technical Program Expanded Abstracts 2015, Society of Exploration Geophysicists, 2015, pp. 4185–4189.

[52] I. Shevchenko and B. Kaltenbacher, *Absorbing boundary conditions for nonlinear acoustics: The Westervelt equation*, Journal of Computational Physics, 302 (2015), pp. 200–221.

[53] ———, *Absorbing boundary conditions for the Westervelt equation*, Conference Publications, 2015.

[54] I. Shevchenko and B. Wohlmuth, *Self-adapting absorbing boundary conditions for the wave equation*, Wave Motion, 49 (2012), pp. 461–473.

[55] G. Simonett and M. Wilke, *Well-posedness and longtime behavior for the Westervelt equation with absorbing boundary conditions of order zero*, Journal of Evolution Equations, 17 (2017), pp. 551–571.

[56] J. Szeftel, *Absorbing boundary conditions for nonlinear scalar partial differential equations*, Computer Methods in Applied Mechanics and Engineering, 195 (2006), pp. 3760–3775.

[57] ———, *A nonlinear approach to absorbing boundary conditions for the semilinear wave equation*, Mathematics of Computation, 75 (2006), pp. 565–594.

[58] T. Walsh and M. Torres, *Finite element methods for nonlinear acoustics in fluids*, Journal of Computational Acoustics, 15 (2007), pp. 353–375.

[59] K. Watanabe, T. Hata, K. Koyama, and H. Kurosawa, *Wave focusing by a spherical concave transducer*, Wave motion, 20 (1994), pp. 1–12.

[60] P. J. Westervelt, *Parametric acoustic array*, The Journal of the Acoustical Society of America, 35 (1963), pp. 535–537.

[61] M. W. Wong, *An introduction to pseudo-differential operators*, World Scientific Publishing, 1999.

[62] F. Wu, Z.-B. Wang, W.-Z. Chen, J. Bai, H. Zhu, and T.-Y. Qiao, *Preliminary experience using high intensity focused ultrasound for the treatment of patients with advanced stage renal malignancy*, The Journal of Urology, 170 (2003), pp. 2237–2240.

[63] Z. Xu, H. Han, and X. Wu, *Adaptive absorbing boundary conditions for Schrödinger-type equations: Application to nonlinear and multi-dimensional problems*, Journal of Computational Physics, 225 (2007), pp. 1577–1589.

[64] R.-C. Ye and X.-F. Jia, *An effective denoising strategy for wave equation migration based on propagation angles*, Applied Geophysics, 9 (2012), pp. 33–40.

[65] K. Yoon and K. J. Marfurt, *Reverse-time migration using the Poynting vector*, Exploration Geophysics, 37 (2006), pp. 102–107.

[66] S. Yoshizawa, T. Ikeda, A. Ito, R. Ota, S. Takagi, and Y. Matsumoto, *High intensity focused ultrasound lithotripsy with cavitating microbubbles*, Medical & Biological engineering & Computing, 47 (2009), pp. 851–860.

[67] Q. Zhang and G. A. McMechan, *Direct vector-field method to obtain angle-domain common-image gathers from isotropic acoustic and elastic reverse time migration*, Geophysics, 76 (2011), pp. WB135–WB149.

E-mail address: muhr@ma.tum.de

E-mail address: vanja.nikolic@ma.tum.de

E-mail address: wohlmuth@ma.tum.de